Biosensors and Bioelectronics 170 (2020) 112675

Contents lists available at ScienceDirect

Biosensors and Bioelectronics

journal homepage: http://www.elsevier.com/locate/bios

Pt-poly(L-lactic acid) microelectrode-based microsensor for in situ glucose detection in sweat

JingYi Han [a], Mingji Li [a,*], Hongji Li [b,**], Cuiping Li [a], Jianshan Ye [c,***], Baohe Yang [a]

[a] Tianjin Key Laboratory of Film Electronic and Communication Devices, Engineering Research Center of Optoelectronic Devices & Communication Technology (Ministry of Education), School of Electrical and Electronic Engineering, Tianjin University of Technology, Tianjin, 300384, PR China
[b] Tianjin Key Laboratory of Organic Solar Cells and Photochemical Conversion, Tianjin Key Laboratory of Drug Targeting and Bioimaging, School of Chemistry and Chemical Engineering, Tianjin University of Technology, Tianjin, 300384, PR China
[c] College of Chemistry and Chemical Engineering, South China University of Technology, Guangzhou, 510641, PR China

ARTICLE INFO

Keywords:
Pt-poly(L-lactic acid) nanoparticles
Biosensor
Interdigital microelectrode array
Sweat glucose
Electrodeposition

ABSTRACT

A miniaturized biosensor was developed for in situ noninvasive detection of glucose in sweat. The biosensor was composed of a pair of interdigital Pt-poly(L-lactic acid) (Pt-PLA) microelectrode arrays operating as the working and auxiliary electrode. The size of the sensor was 3.56 × 0.72 mm, while the width of the interdigital microelectrodes was 2.4 μm. The microelectrodes with densely packed coral-like Pt-PLA nanoparticles were fabricated using a multi-potential step deposition process. We investigated the influence of the Pt-PLA electrodeposition time on the morphology and electrochemical performance of the microelectrode. The optimized biosensor exhibited high electrocatalytic activity because of the synergistic effects between the Pt nanoparticles and PLA polymer matrix, including the electrooxidation of Pt on glucose, the adsorption of glucose by the PLA polymer, and the acceleration of the glucose dehydrogenation step. For glucose detection in sweat and tears, the linear concentration ranges were observed to be 0.001–33.76 μM and 33.76–1000 μM, with a low detection limit of 0.19 nM. The miniaturized biosensor exhibited high sensitivity and signal stability, and could be suitable for use in the long-term monitoring of sweat glucose levels in patients, athletes, and other subjects in various difficult environments.

1. Introduction

In recent times, the application of miniaturized biosensors for the in situ monitoring of biomarkers in body fluids is becoming an important field of study for researchers. Miniaturized biosensors are directly attached onto the skin or inserted into the body to obtain biosignals such as glucose level, dopamine level, and blood pressure. Such biosensors can be embedded within human tissues or clothing (Cao et al., 2020). Miniaturized electrochemical sensors are trending because of the increasing demand for devices that are capable of monitoring chemical substances in gases or liquids in real-time. Modern microelectrodes can be disk-shaped (Yuan and Wang, 2020), cylindrical (Alwarappan et al., 2007; Li et al., 2009), and needle-shaped (Zhang et al., 2019). Furthermore, the microelectrodes can be arranged in rectangular arrays, spiral arrays, concentric circles, parallel arrays, and interdigitated microelectrode (IDME) arrays (Ferguson et al., 2019; Jasim et al., 2019; Liu et al., 2020; Toi et al., 2019). Among these, the IDME arrays are used as the working and auxiliary electrodes, and the interdigital fingers of the two microelectrode arrays are interlaced with each other, creating a compact structure for the sensor (Jasim et al., 2019). Using tens to hundreds of interdigital pairs could effectively amplify the detection signals in the microsensors, which would be conducive to the realization of high electrocatalytic oxidation and high selectivity functions. Generally, the size of interdigitated electrodes (IDEs) used in electrochemical sensors ranges from approximately tens of microns to several hundred microns (Zhang et al., 2020). These IDEs have relatively large dimensions. Photolithography can be used to fabricate metal IDME arrays of the order of hundreds of nanometers to several microns. However, common modification processes such as heating, cross-linking, and acid/base etching can easily damage the IDME array structure, making it

* Corresponding author.
** Corresponding author.
*** Corresponding author.
E-mail addresses: limingji@163.com, limingji@tjut.edu.cn (M. Li), hongjili@yeah.net, lihongji@tjut.edu.cn (H. Li), jsye@scut.edu.cn (J. Ye).

https://doi.org/10.1016/j.bios.2020.112675
Received 3 August 2020; Received in revised form 25 September 2020; Accepted 1 October 2020
Available online 7 October 2020

difficult for the films to be compatible with such micro-nano processing technologies. Therefore, the development of a sensing layer deposition method compatible with the fabrication process of micro-nano devices would enhance the process of miniaturization of electrochemical biosensors.

Human sweat (perspiration) is an inherent body fluid, and the level of such biomarkers can be monitored noninvasively (Xiong et al., 2018; Zahed et al., 2020). Generally, glucose cannot penetrate the skin; therefore, the glucose levels in sweat is extremely low. However, for people with diabetes or abnormal metabolism, the glucose content in their sweat or tears is higher than normal. According to reports in the literature, the glucose content in sweat could vary from 5 μM to 2 mM (Karpova et al., 2019). Furthermore, sweat contains glucose that can accurately reflect the blood glucose levels (Moyer et al., 2012). Therefore, in situ noninvasive monitoring of glucose levels in sweat is essential for the tracking of human health and clinical diagnosis of various diseases.

In recent times, electrochemical sensors of the enzyme- and non-enzyme types, capable of detecting sweat glucose, have been developed by researchers (Bhide et al., 2018; Karpova et al., 2019; Oh et al., 2018; Toi et al., 2019; Xia et al., 2020; Yoon et al., 2020). Sweat glucose sensors are generally made of flexible materials, which enhance the adhesion of the sensor with the skin. Enzyme-based sensors receive a selective response to the glucose through an immobilized enzyme (GOx), such as glucose oxidase (GOx)-horseradish peroxidase/carbon nanotubes-ethylene-vinyl acetate copolymer (Xia et al., 2020), GOx/Pt nanoparticles (NPs)/acetic acid-treated porous laser-induced graphene (Yoon et al., 2020), and GOx-Au-ZnO/porous polyamide biosensors (Bhide et al., 2018). However, enzymes are sensitive to environmental conditions, and enzyme activities diminish over time (Oh et al., 2018; Toi et al., 2019). One of the applications of noninvasive sweat glucose detection is the long-term in situ monitoring of glucose levels in humans. Transition metals such as Au, Pt, Ni, Cu and their oxides can directly oxidize glucose (Savk et al., 2019; Wang et al., 2020; Wu et al., 2019). The application of non-enzymatic electrochemical biosensors in glucose detection has been extensively studied (Savk et al., 2019; Toi et al., 2019; Wu et al., 2019). Moreover, researchers have proposed non-enzymatic glucose sensors, based on electrocatalytic nanomaterials such as Au and Cu, for the purpose of sweat glucose detection (Oh et al., 2018; Toi et al., 2019).

In this study, we report on an IDME-based electrochemical biosensor for the detection of glucose in human sweat. We proposed the fabrication of miniaturized enzyme-free biosensors using a controllable electrodeposition technique, which could be used to deposit catalytic nanomaterials on commercial microdevices or replace the structural units in the same. The method of fabricating a biosensor based on commercial microdevices can be effective for the integration of the sensor with other functional units, which is essential for the multi-functionalization of the microsensor. The miniaturized sensor consisted of two sets of interdigital Pt-PLA microelectrode arrays integrated on a quartz substrate, with an interdigital width of 2.4 μm. Densely packed coral-shaped Pt-PLA nanospheres were used to fabricate the interdigital microelectrodes. Platinum is highly compatible with the human body, and has the ability to oxidize glucose under human physiological conditions (Ayranci et al., 2019; Caglar et al., 2020; Zhiani et al., 2020). PLA is a biodegradable polymer that is highly safe for the human body and does not cause any toxic or side effects. Moreover, a coordination compound can be formed between PLA and Pt, which could result in the formation of a Pt-PLA nanocomposite network structure. Although the miniaturized biosensor fabricated in this study was extremely small, the current in response to the glucose was significantly high. Moreover, the limit of detection (LOD) was as low as 0.19 nM, and only 1–5 μL of sweat or teardrops were sufficient to detect glucose. Furthermore, this sensor could be integrated with wearable devices that can be hidden and attached to various parts of the human body, such as fingers, wrists, and scalp.

2. Experimental section

The experimental materials and characterization methods are provided in the Supporting Information (SI).

2.1. Fabrication of the Pt-PLA IDME-based sensor

Aluminum (Al) IDME arrays, with a two-electrode system, were fabricated on a quartz substrate (3.56 × 0.72 × 0.41 mm) by the process of photolithography (433 MHz surface acoustic wave device). Each Al microelectrode array, having 162 microelectrodes (2.4 μm in width, 180 μm in length), was distributed in parallel at equal intervals of 1.3 μm (Fig. 1A and Fig. S1). The Pt-PLA IDME-based sensor was prepared in a single step using an ectrochemical multipotential step method with Al IDME array as template (Fig. 1B, Figs. S2 and S3). The details of the experiment are described in the SI.

3. Results and discussion

3.1. Sensor characterization

Fig. S1 shows the optical microscopic (OM), scanning electron microscopic (SEM), and atomic force microscopic (AFM) images of the Al microelectrodes. The Al microelectrodes showed a smooth surface (Fig. S1), whereas the surface of the Pt-PLA microelectrodes was observed to be rough (Fig. 2A). The enlarged SEM image showed that the Pt-PLA microelectrodes were composed of a large number of nanoparticles (Fig. S4). The spherical nanoparticles exhibited a coral-like appearance, and the size of each nanosphere varied from approximately 100 to 500 nm (Fig. 2B and Fig. S4). The coral-like three-dimensional nanospheres had a large specific surface area with multiple analyte absorption channels, which was beneficial for increasing the electrocatalytic activity (Liu et al., 2018). Furthermore, a high-resolution transmission electron microscopic (TEM) image of the nanoparticles is shown in Fig. 2C, wherein clear crystal lattice fringes can be seen with d-spacings of approximately 0.23 and 0.2 nm, attributed to the (111) and (200) lattice planes of the Pt crystals (Gao et al., 2018; Jin et al., 2017). Furthermore, the fast Fourier transform (FFT) image of the area marked by the red arrow in Fig. 2B also reveals the (111) and (002) planes of the Pt crystals (Fig. 2C right).

Fig. 2D shows the SEM image of the Pt-PLA microelectrode and the corresponding energy-dispersive X-ray spectroscopic (EDX) element mapping distribution patterns of Pt, C, Al, O, and Si atoms (C atoms belonged to the PLA, Al was derived from the original Al microelectrode, O atoms were obtained from the PLA and quartz substrate (SiO_2), and the Si atoms belonged to the quartz substrate). The Pt and C atoms were mainly distributed on the microelectrode, while the Al and O atoms covered the entire surface of the sample. Further, the TEM image of the nanosphere and the corresponding EDX element mapping distributions are shown in Fig. 2E. The nanosphere was composed of Pt, C, Al, O, and Si atoms, with mass fractions of 73.76%, 13.56%, 2.43%, 7.77%, and 2.48%, respectively. After undergoing the Pt-PLA electrodeposition process, traces of etching appeared on the quartz surface (Fig. S5). The etched Si and Al atoms were incorporated into the Pt-PLA nanoparticles in small amounts. This might have enhanced the firm bonding of the microelectrode array on the quartz substrate.

Survey and high-resolution X-ray photoelectron spectroscopic (XPS) spectra of the Pt-PLA microelectrodes are shown in Fig. 2F. The signals corresponding to Pt, C, O, Al, and Si were observed for the Pt-PLA microelectrodes. The peaks of Pt $4d_5$ and Pt $4d_3$ appeared at approximately 315.2 and 332.2 eV, respectively, and were consistent with the characteristic peaks of Pt as reported in the literature (Zhao et al., 2011). The C 1s peak was deconvoluted into three peaks at 284.8, 286.4, and 289.0 eV. The peak at 284.8 eV was characteristic of the C–C and C–H bonds in PLA. Similarly, the peak at 286.4 eV was characteristic of the C–O/or C–O–C bonds, and the binding energy of 289.0 eV was due to the O═C

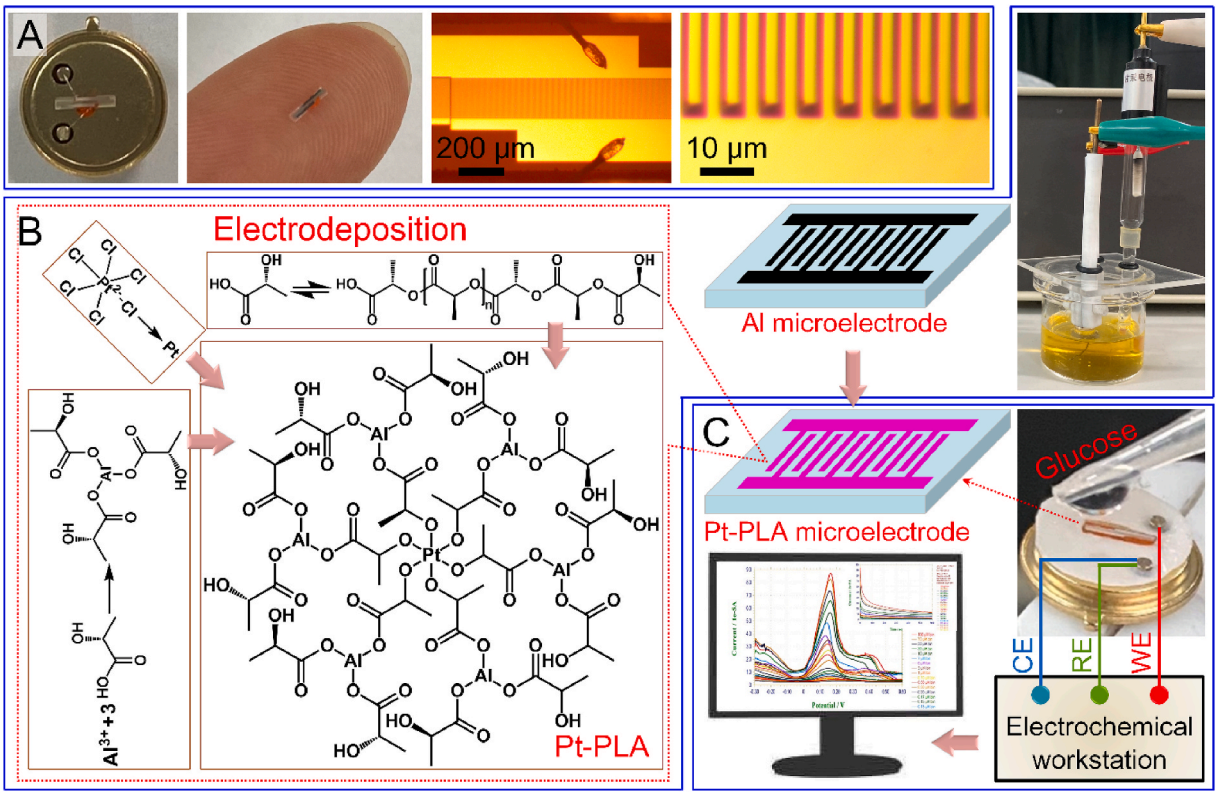

Fig. 1. (A) Photographs and OM images of a patch microelectrode array sensor. (B) Schematic diagrams of the electrodeposition method and synthesis of the sensitive film. (C) Method for detecting the glucose response signal using microelectrode array sensor.

bonds in PLA or the adsorbed carbonate from the environment (Li et al., 2020; Majchrowicz et al., 2020). The high resolution XPS spectrum of Al 2s showed two peaks at the binding energies of 117.1 eV and 119.5 eV, respectively, which were consistent with the Al in the Al (III) state (Taherkhani and Soltanieh, 2020). The O 1s peak appeared at a binding energy of 532.3 eV. The O signal mainly belonged to the oxygen components of the quartz substrate (SiO_2) and the PLA. An additional signal of Si 2p at 102.9 eV was obtained due to the presence of the quartz substrate (SiO_2). The XPS and EDX composition analysis confirmed that the Pt-PLA NPs, with a small amount of Al, were closely packed to form the microelectrodes.

3.2. Pt-PLA microelectrode assembly and condition optimization

The preparation of the Pt-PLA microelectrode included the oxidation of Al, the reduction of Pt in H_2PtCl_6, the oxidation polymerization of LA, and the coordination reaction of Pt and Al with LA (or PLA), as shown in Fig. 1B and SI (2.1). Under electrocatalysis using a pulsed electrical signal of 0.5 s, the Al atoms of the Al microelectrode array slowly oxidized and coordinated with LA to form aluminum lactate ($C_9H_{15}AlO_9$). The Pt-PLA NPs were deposited at −2 V. The O atoms of PLA and $C_9H_{15}AlO_9$ coordinated with the Pt NPs to form the coral-like Al-doped Pt-PLA composite (Pt-PLA).

As the pulsed potential was set to 0.5 V, the Pt-PLA NPs were irregularly distributed on the entire substrate, indicating that the Al consumption was too fast, and did not serve as a template for the nucleation of the Pt-PLA NPs (Fig. S6A and B). Although most of the NPs were deposited on the microelectrode area, lowering the potential to 0.2 V made the distribution of the NPs uneven, indicating a high Al dissolution rate (Fig. S6C and D). On lowering the potential to 0 V, a significant amount of Pt-PLA NPs of uniform size were deposited, and the Al microelectrodes were completely retained (Fig. S6E and F). As the potential was reduced to −0.2 V, the NPs closely stacked along the Al region to form regular Pt-PLA microelectrodes (Fig. 2A).

In addition, the deposition time of Pt-PLA was optimized. A PLA layer was formed on the surface of the Al microelectrodes (Fig. S7A and B) after 50 cycles. After 100 deposition cycles, small Pt-PLA NPs were observed on the microelectrodes (Fig. S7C and D). The Pt-PLA microelectrodes were formed after 150 cycles of deposition (Fig. 2A). On further increasing the number of depositions to 200 cycles, Pt-PLA particles were also deposited on the quartz substrate to join the two sets of microelectrodes (Fig. S7E and F).

We investigated the electrochemical performance of the sensor. Electrochemical impedance spectra (EIS) (Fig. 3A and B) and cyclic voltammetry (CV) curves (Fig. 3C) were recorded for a 0.05 M KCl solution containing 0.5 mM $[Fe(CN)_6]^{3-/4-}$. For the semicircle in the high-frequency region of the Nyquist plots (Fig. 3A), the intercept on the real part is related to the series resistance (R_s), while the diameter reflects the electron transfer resistance (R_{ct}) at the electrode/electrolyte interface, as shown in Fig. 3B. The illustration shows the equivalent circuit of the sensor. The R_s value gradually decreased as the number of depositions increased from 50 to 150 cycles, and increased significantly after 200 cycles of deposition (in order: 13.88, 4.70, 4.30, and 5.89 Ω cm^2). For sensors with 50–150 cycles of electrodeposition, the R_{ct} values obtained were 1.17, 15.39, 0.14, and 94.79 Ω cm^2, respectively. For the Pt-PLA microelectrode deposited in the case of 150 cycles, the R_s value was 4.30 Ω cm^2 while the R_{ct} value was 0.14 Ω cm^2, which was considered the most suitable impedance state among the four Pt-PLA microelectrode sensors. The CV curves were then recorded at a scan rate of 50 mV s^{-1} (Fig. 3C). The deposition cycle was increased from 50 to 150 cycles, and the Faraday current was significantly improved. However, the current decreased after 200 cycles of electrodeposition, which indicated that the 150-cycle Pt-PLA microelectrode exhibited the highest electron transfer efficiency and was consistent with the EIS results. The differential pulse voltammetry (DPV) curves were then recorded for the 200 μM glucose solution to compare the four sensors (Fig. 3D), and it was

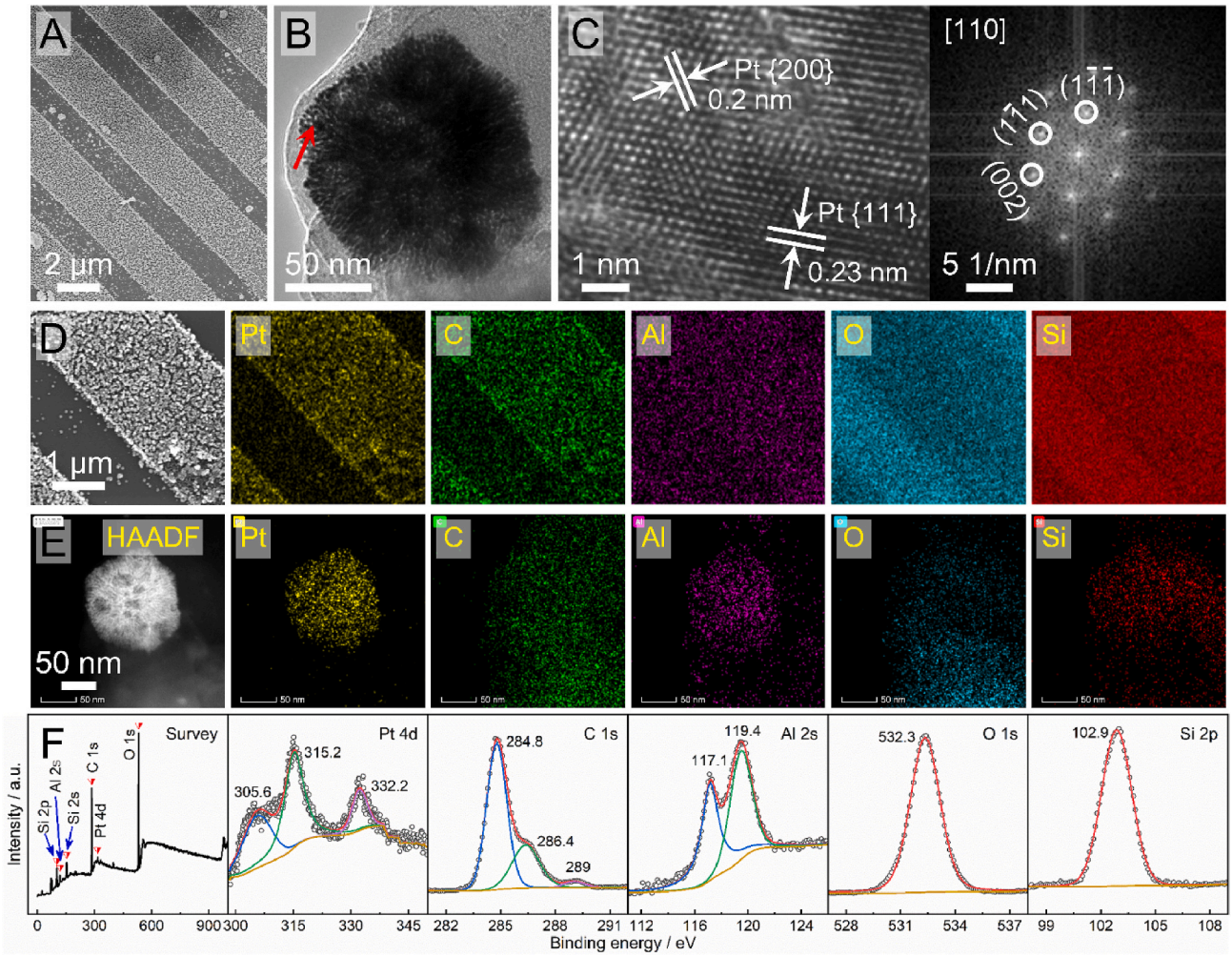

Fig. 2. (A) SEM image of the Pt-PLA microelectrode array. (B) TEM image and (C) High-resolution TEM image (red arrow-pointed area in (B)) of the Pt nanoparticles, as well as the fast Fourier transform (FFT) pattern corresponding to (C). (D) SEM image of the Pt-PLA microelectrode, and the corresponding EDX element mapping distribution patterns of Pt, C, Al, O, and Si. (E) TEM image of a Pt-PLA nanoparticle and the corresponding EDX element mapping distribution patterns of Pt, C, Al, O, and Si. (F) Survey, Pt 4d, C 1s, Al 2s, O 1s, and Si 2p core XPS spectra of the Pt-PLA microelectrodes. (For interpretation of the references to colour in this figure legend, the reader is referred to the Web version of this article.)

observed that the 150-cycle Pt-PLA microelectrode sensor showed the highest glucose response current. By comparing the EIS, CV, and the glucose response in the DPV curve, we inferred that the 150-cycle Pt-PLA microelectrode sensor could be the used as the optimal device for sweat glucose detection.

For the optimized Pt-PLA microelectrode sensor, we investigated the effect of pH on the glucose response (Fig. 3E). On adjusting the artificial sweat to a pH range of 3.4–7.5, the peak potential gradually shifted towards the negative potential (Fig. 3F). This indicated the transfer of protons (H^+) during the electrochemical reaction. The glucose response mechanism of the sensor was observed to be a direct electron transfer process, which involved the formation of $Pt(OH)_{ads}$, and the oxidation of the hemiacetal group of glucose by $Pt(OH)_{ads}$ (Toi et al., 2019; Zhang et al., 2018). In detail, the hydrogen bonded to C_1 in the hemiacetal group was the first to be oxidized on the Pt surface, forming redical species; these redical species were further oxidized to generate gluconolactone, and transfer two electrons to the sensing electrode (Madhuvilakku et al., 2018; Wang et al., 2020). The main reaction equations are as follows:

$$Pt + H_2O \rightleftharpoons Pt - OH_{ads} + H^+ + e^- \quad (1)$$

$$C_6H_{12}O_6\ (\text{Glucose}) \xrightarrow{Pt-OH_{ads}} C_6H_{10}O_6\ (\text{Gluconolactone}) + 2H^+ + 2e^- \quad (2)$$

Furthermore, the sensor showed the highest current at a pH 6.6, and showed a relatively high response current at a pH of 7.0. The pH of human sweat is approximately neutral. Therefore, we performed a calibration experiment at a pH of 7.0.

3.3. Glucose detection

We performed a quantitative glucose analysis using DPV and amperometric response (I-t) (Fig. 4). As shown in Fig. 4A and Fig. S8A, the peak current of the DPV curve gradually increased with the increase in glucose concentration in the range of 0.01–100 μM. Furthermore, two linear relationship curves could be fitted between the logarithmic glucose concentration and the peak current (0.01–0.105 μM; 0.105–100 μM) (Fig. 4B). This result indicated that the biosensor showed a high electrocatalytic response to the glucose.

A series of I-t curves were recorded for different concentrations of glucose (Fig. S8B). The working electrode area of the Pt-PLA microelectrode sensor was approximately 0.3 mm^2, and the droplet volume was 5 μL (left inset). The collection time of the DPV curve was approximately 23 s. We selected a curve region of 20–30 s, having a high response and a stable current range, to formulate a quantitative glucose detection model. The I-t curve shown in Fig. 4C represents the 20–30 s segment in Fig. S8B. The central inset in Fig. 4C shows the linear

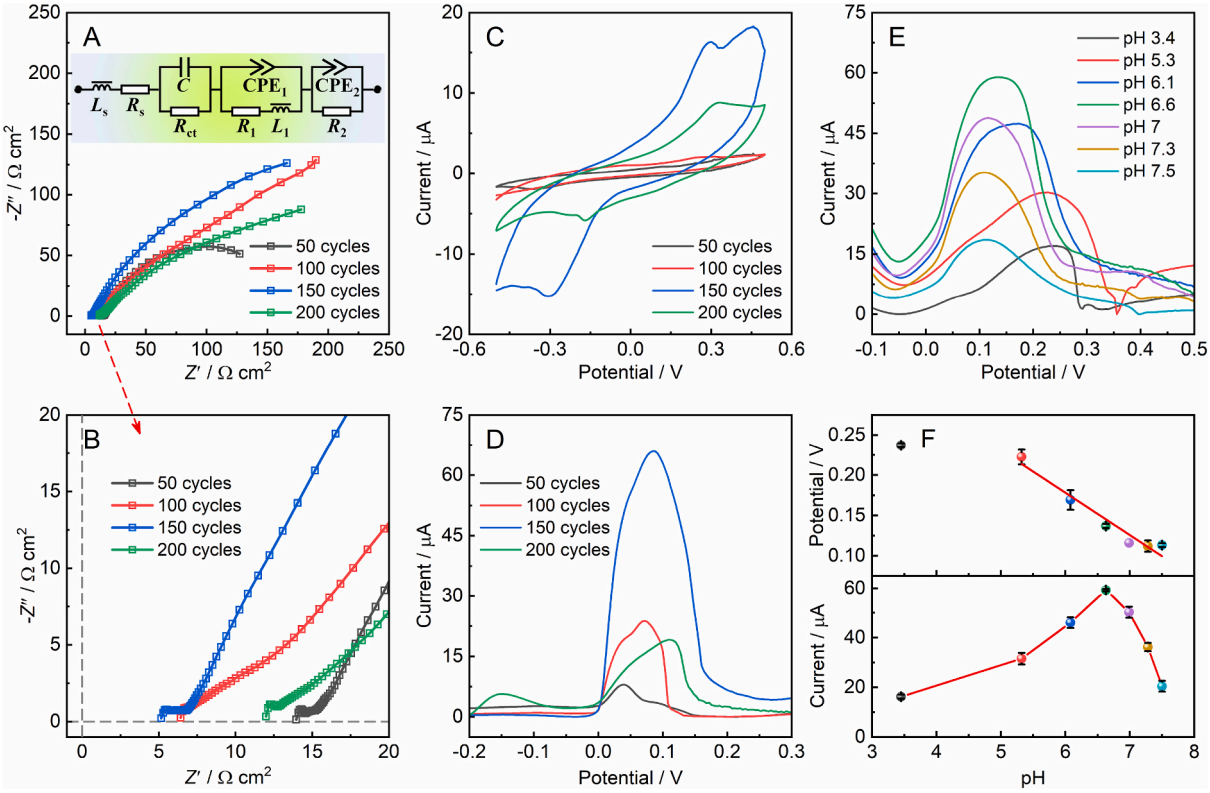

Fig. 3. Electrochemical properties of the Pt-PLA microelectrodes with cycle times of 50, 100, 150 and 200 cycles for electrodeposition. (A) Nyquist plots for 0.05 M KCl containing 0.5 mM $[Fe(CN)_6]^{3-/4-}$. The frequency range is from 1 Hz to 1000 kHz. (B) The enlarged high-frequency region in (A). (C) CV curves for 0.05 M KCl containing 0.5 mM $[Fe(CN)_6]^{3-/4-}$ at scan rate of 50 mV s^{-1}. (D) DPV curves for 5 μM glucose solution. (E) DPV curves representing artificial sweat with different pH values, containing 5 μM glucose (150 cycles). (F) Curves indicating the influence of pH value on the peak current and peak potential.

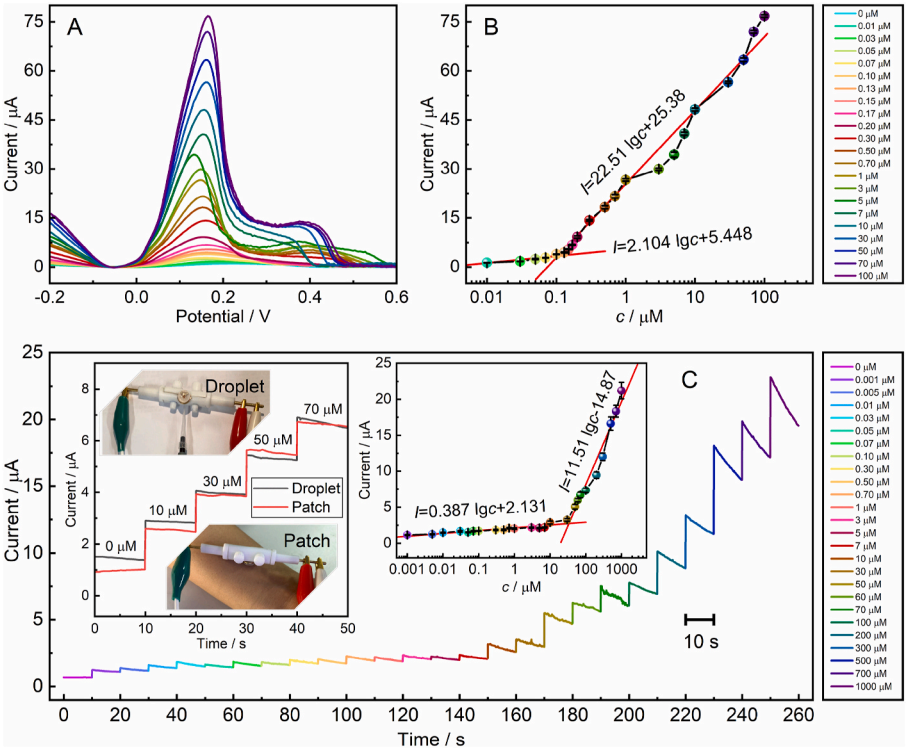

Fig. 4. (A) DPV curves of the Pt-PLA microelectrode in 0.1 M PBS (pH 7.0), containing different concentrations of glucose (0, 0.01–100 μM) in artificial sweat. (B) Working curve and linear regression equation from (A). (C) Amperometric responses in the range of 20–30 s, obtained by using Pt-PLA microelectrodes in artificial sweat containing different concentrations of glucose (0, 0.001–1000 μM). The illustration to the left shows the amperometric response curves recorded for the two detection methods: dropwise addition, and skin attachment. The illustration to the right shows the working curve and linear regression equation.

relationship between the response current and the logarithmic glucose concentration. In the glucose concentration range of 0.001–33.76 μM, the linear regression equation was $I = 0.387\ lgc + 2.131$ (μA; μM), $R = 0.920$. Similarly, the linear regression equation was found to be $I = 11.51\ lgc - 14.87$ (μA; μM), $R = 0.980$, for the concentration range of 33.76–1000 μM. The glucose response sensitivity was 0.387 μA (l g μM)$^{-1}$ for a low concentration range of 0.001–33.76 μM; whereas, the sensitivity was observed to be 11.51 μA (l g μM)$^{-1}$ for a high concentration range of 33.76–1000 μM. The LOD was estimated to be 0.19 nM, according to the formula LOD = 3σ/s, where σ is the standard deviation of the blank signal (n = 10) and s is the sensitivity. These results indicated that the sensor was glucose-sensitive and showed trace glucose detectability.

We compared the current signals, obtained by the sensor, using the dropwise addition method and by attaching the sensor onto the skin. A number of I-t curves were obtained for artificial sweat, with and without different concentrations of glucose (Fig. S9). The first method involved directly measuring the signal after dropping 5 μL of solution onto the sensor. The second method involved measuring the electrical signals by placing the sensor (with 5 μL of the solution) inverted and close to the skin (left inset in Fig. 4C). The difference between the current signals obtained by the two methods was observed to be less than 5%. This indicated that the linear regression equation established by the dropwise addition method could be used to calculate the glucose concentration in sweat formed on the skin. A list of various sweat glucose sensors and IDME array sensors, comparing their sensor and electrode size, linear concentration range, and LOD, are presented in Table S1. Compared to the other sweat glucose sensors, the Pt-PLA IDME-based sensor was extremely small (smaller than other IDE sensors) and showed a LOD approximately three orders of magnitude lower than that of the other sensors; however, the concentration range and response current obtained were similar.

3.4. Detection of human sweat and tears

We determined the glucose level in human sweat and teardrops to verify the feasibility of the practical application of Pt-PLA microelectrode array sensors. Fig. 5A and Fig. S10 show the I-t curves obtained from the human sweat and glucose-added human sweat. Sweat was collected from different volunteers (average age, 24 years). The glucose levels in the sweat of these volunteers were in the range of 0.05–41.00 μM (Figs. S10 and S11). The amount of sweat collected from three of the volunteers was relatively large, which was used for the spike-and-recovery experiment. The glucose responses detected by the sensor were observed to be 102%, 92.6% and 102.6% (Fig. 5B). Because the recoveries were in the range of 90%−110%, the glucose detection result of the microelectrode sensor was accurate.

Fig. S12A shows the I-t curves obtained by attaching the sensor onto the wrists of five volunteers. For the five volunteers, the blood glucose levels recorded using the commercial blood glucose meter were approximately 150 times greater than the sweat glucose levels measured using the PLA-Pt microsensor (Fig. 5C). This indicated that a correlation existed between the glucose levels in sweat and blood sugar. Fig. S12B and Fig. 5D show the I-t curves and calculated glucose concentrations obtained using the PLA-Pt microsensor, in a serum sample diluted 100 times. The average glucose level in the diluted serum was 35.35 ± 1.40 μM, i.e., the serum glucose concentration was about 3.54 mM. Additionally, the blood glucose value measured by the blood glucose meter was 3.4 mM. The glucose test results of the PLA-Pt microsensor and blood glucose meter were similar, which indicated that the detection results of the PLA-Pt microsensor were accurate. Fig. 5E shows the I-t curves of the tear droplets detected by the sensor. The concentration of glucose in the human tears ranged from 0.05 to 49.48 μM (Fig. 5F). Tears and sweat were collected from different volunteers at different instances of time; however, the glucose concentration range was similar in all cases. The sweat detection and teardrop collection processes are shown in Videos 1 to 4 in SI.

3.5. Reproducibility, selectivity, and stability of the Pt-PLA microelectrode array sensor

Human sweat and tears contain NaCl, KCl, $CaCl_2$, urea, and lactic acid. A series of DPV curves were obtained using the Pt-PLA microsensor, representing a 0.7 μM glucose solution and a 0.7 μM glucose solution containing 0.01 M NaCl, KCl, $CaCl_2$, urea, and lactic acid (Fig. S13). The change in concentrations of the aforementioned

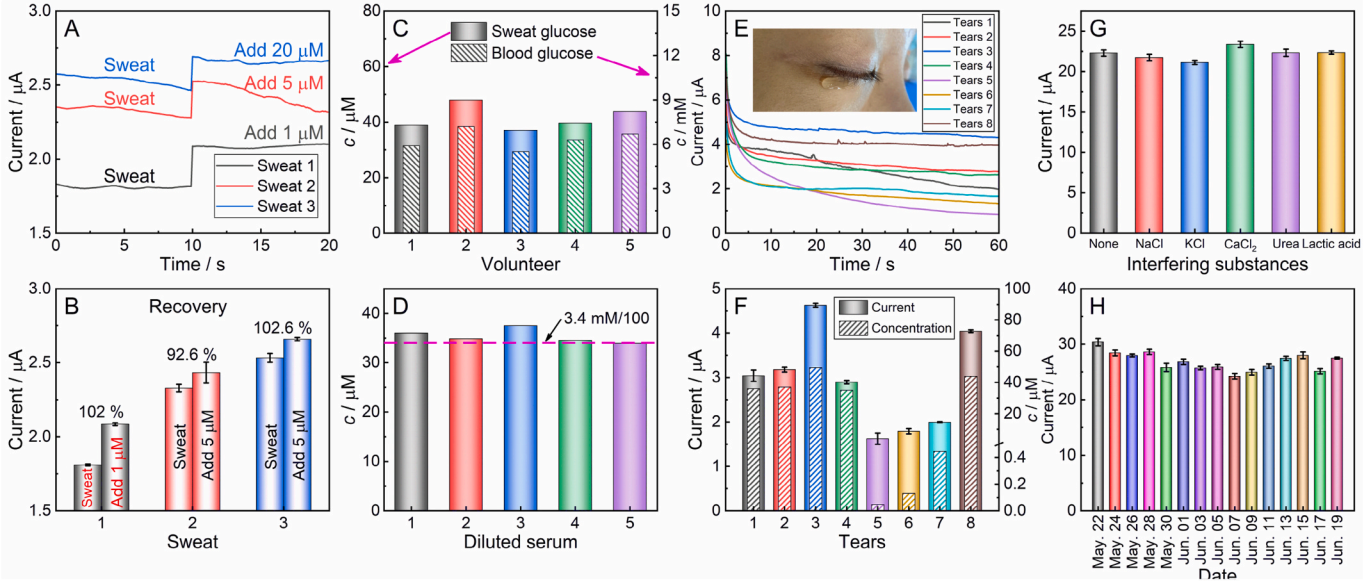

Fig. 5. (A) Amperometric response curves of human sweat, and a mixture of human sweat and glucose with different concentrations, obtained by dropping 5 μL of the sample onto the Pt-PLA microelectrode sensor (showed by the curve segments of 20–30 s). (B) Glucose recoveries from the sweat of different volunteers. (C) Glucose concentration in sweat (obtained by the sensor) and blood (measured by a blood glucose meter) of the five volunteers. (D) Glucose concentration of the diluted serum (1/100 vol ratio) detected by the Pt-PLA microsensor. (E) Amperometric response curves of glucose in tears and (F) the corresponding response curves for current and glucose concentrations. (G) Anti-interference ability and (H) long-term stability of the sensor.

compounds, with respect to the glucose response current, was observed to be less than 5% (Fig. 5G). Furthermore, five sensors were used to obtain the DPV curves for a 3 μM glucose solution (Fig. S14). It was observed that the difference between the peak currents obtained by using the five sensors was also less than 5%. The long-term stability of the sensor was investigated by measuring the DPV curves for the 3 μM glucose droplets every two days (Fig. S15). After a month of observation, the amount of fluctuation in the peak current was found to be in the range of 5.7–10.2%, and the final signal retention value was 90.6% of the initial value (Fig. 5H). These results confirmed that the sensor possessed high selectivity, anti-interference ability, reproducibility, and excellent long-term stability.

4. Conclusion

A miniaturized electrochemical biosensor, based on IDME arrays, was prepared for the detection of glucose in human sweat via multipotential step electrodeposition. The micro-biosensor was composed of two sets of Pt-PLA IDME arrays. A total of 162 microelectrodes, having a width of 2.4 μm, were connected to form a comb-shaped microelectrode array. Each microelectrode was densely packed with Pt-PLA nanoparticles, and showed high electrochemical activity for glucose detection. For the detection of glucose in sweat, a detection concentration range of 0.001–1000 μM, and a detection limit of 0.019 nM was chosen. The proposed quantitative detection model was suitable for both the detection methods (dropwise addition and skin attachment). The miniaturized enzyme-free biosensor showed high sensitivity towards the glucose response, and exhibited high stability. Therefore, the sensor could be efficiently used for the noninvasive measurement of glucose levels in human sweat and tears. This study proposes a novel method for the fabrication of IDME array-based microsensors using the process of electrodeposition. Microsensors with different electrocatalytic materials could be constructed using this method. The development of a sensor array composed of microsensors that could be integrated on a circuit board, to develop a continuous sweat monitoring system for the simultaneous detection of multiple biomarkers in human sweat, remains a future prospect.

CRediT authorship contribution statement

JingYi Han: Conceptualization, Investigation. **Mingji Li:** Methodology, Writing - review & editing, Supervision. **Hongji Li:** Investigation, Data curation, Writing - original draft, preparation. **Cuiping Li:** Formal analysis. **Jianshan Ye:** Validation, Resources. **Baohe Yang:** Supervision.

Declaration of competing interest

The authors declare that they have no known competing financial interests or personal relationships that could have appeared to influence the work reported in this paper.

Acknowledgements

This work was supported by the Key Realm R&D Program of Guangdong Province of China (No. 2019B020219002) and the Natural Science Foundation of Tianjin City (No. 17JCZDJC32600).

Appendix A. Supplementary data

Supplementary data to this article can be found online at https://doi.org/10.1016/j.bios.2020.112675.

References

Alwarappan, S., et al., 2007. Sensor. Actuator. B Chem. 128, 299–305.
Ayranci, R., et al., 2019. Mater. Sci. Eng. C 99, 951–956.
Bhide, A., et al., 2018. Biosens. Bioelectron. 117, 537–545.
Caglar, A., et al., 2020. Int. J. Hydrogen Energy 45, 490–500.
Cao, M.S., et al., 2020. Adv. Mater. 32, e1907156.
Ferguson, M., et al., 2019. Adv. Healthcare Mater. 8, e1900558.
Gao, Z., et al., 2018. Carbon 139, 369–377.
Jasim, I., et al., 2019. Biosens. Bioelectron. 126, 292–300.
Jin, L.H., et al., 2017. ACS Appl. Mater. Interfaces 9, 10027–10033.
Karpova, E.V., et al., 2019. Anal. Chem. 91, 3778–3783.
Li, C.-Z., et al., 2009. Am. J. Biomed. Sci. 1, 274–282.
Li, R., et al., 2020. Mater. Chem. Phys. 241, 122338.
Liu, C., et al., 2020. Talanta 212, 120801.
Liu, X., et al., 2018. Sensor. Actuator. B Chem. 266, 853–860.
Madhuvilakku, R., et al., 2018. Anal. Chim. Acta 1042, 93–108.
Majchrowicz, A., et al., 2020. Arch. Civ. Mech. Eng. 20, 50.
Moyer, J., et al., 2012. Diabetes Technol. Therapeut. 14, 398–402.
Oh, S.Y., et al., 2018. ACS Appl. Mater. Interfaces 10, 13729–13740.
Savk, A., et al., 2019. Sci. Rep. 9, 19228.
Taherkhani, K., Soltanieh, M., 2020. Surf. Coating. Technol. 393, 125820.
Toi, P.T., et al., 2019. ACS Appl. Mater. Interfaces 11, 10707–10717.
Wang, T.P., et al., 2020. Appl. Catal., B 260, 118140.
Wu, L., et al., 2019. Biosens. Bioelectron. 135, 45–49.
Xia, H.Q., et al., 2020. Sensor. Actuator. B Chem. 312, 127962.
Xiong, C., et al., 2018. Biosens. Bioelectron. 101, 21–28.
Yoon, H., et al., 2020. Sensor. Actuator. B Chem. 311, 127866.
Yuan, F., Wang, Z.G., 2020. Microelectron. J. 96, 104686.
Zahed, M.A., et al., 2020. Biosens. Bioelectron. 160, 112220.
Zhang, C.M., et al., 2018. ACS Omega 3, 96–105.
Zhang, D., et al., 2020. Nano Energy 67, 104251.
Zhang, Y., et al., 2019. Sensor. Actuator. B Chem. 301, 127126.
Zhao, Y., et al., 2011. Chem. Eng. J. 170, 440–444.
Zhiani, M., et al., 2020. Int. J. Hydrogen Energy 45, 13496–13507.